

## APOSTLE OBSERVATIONS OF GJ 1214b: SYSTEM PARAMETERS AND EVIDENCE FOR STELLAR ACTIVITY

P. KUNDURTHY, E. AGOL, A. C. BECKER, R. BARNES<sup>1</sup>, B. WILLIAMS, AND A. MUKADAM

Astronomy Department, University of Washington, Seattle, WA 98195, USA

Received 2010 November 18; accepted 2011 February 21; published 2011 April 1

### ABSTRACT

We present three transits of GJ 1214b, observed as part of the Apache Point Observatory Survey of Transit Light Curves of Exoplanets. By applying Markov Chain Monte Carlo techniques to a multi-wavelength data set which included our *r*-band light curves and previously gathered data of GJ 1214b, we confirm earlier estimates of system parameters. Using spectral energy distribution fitting, mass–luminosity relations, and light curve data, we derived absolute parameters for the star and planet, improving uncertainties by a factor of two for the stellar mass ( $M_{\star} = 0.153^{+0.010}_{-0.009} M_{\odot}$ ), stellar radius ( $R_{\star} = 0.210^{+0.005}_{-0.004} R_{\odot}$ ), planetary radius ( $R_p = 2.74^{+0.06}_{-0.05} R_{\oplus}$ ), and planetary density ( $\rho_p = 1.68 \pm 0.23 \text{ g cm}^{-3}$ ). Transit times derived from our study show no evidence for strong transit timing variations. We also report the detection of two features in our light curves which we believe are evidence for a low-energy stellar flare and a spot-crossing event.

*Key words:* methods: statistical – planetary systems – stars: activity – stars: fundamental parameters

*Online-only material:* color figures, machine-readable table

### 1. INTRODUCTION

Exoplanets detected using both transits and the radial velocity (RV) technique offer the unique opportunity to measure many of their physical properties. Transits can place limits on the radius of an exoplanet given the radius of the star, and transits can also constrain orbital parameters such as inclination and orbital period. When coupled with RV measurements, we can constrain the mass ( $M_p$ ) and the average density of a planet ( $\rho_p$ ). We may therefore probe the interiors of transiting exoplanets and constrain bulk composition and formation models (Guillot 2005; Fortney et al. 2008; Torres et al. 2008; Baraffe et al. 2008). Here we present and interpret three light curves of the transiting planet GJ 1214b (Charbonneau et al. 2009), a planet unlike any in our solar system.

Prior to 2009, all transiting exoplanets were found with radii consistent with the giant planets in our solar system, i.e., they had gaseous envelopes. As surveys improved, they began to reach sensitivities which could detect smaller rocky planets. In our solar system, Neptune has a mass of  $17 M_{\oplus}$  while the Earth is the largest terrestrial planet, suggesting that the transition mass between rocky and gaseous planets lies somewhere between these values. With no such “transition” object in the solar system, we must rely on theory, which predicts that  $\sim 10 M_{\oplus}$  is the critical mass (Pollack et al. 1996), although it could be as low as  $2 M_{\oplus}$  (Ikoma et al. 2001) or as high as  $16 M_{\oplus}$  (Lissauer et al. 2009). The  $10 M_{\oplus}$  limit should therefore be seen as a sort of median of theoretical results, and not as a true boundary between rocky and gaseous worlds. The discovery of transiting planets between 1 and  $17 M_{\oplus}$  therefore provides critical insight into the planet formation process.

Two transiting planets are now known with  $1 M_{\oplus} \leq M_p \leq 10 M_{\oplus}$ , CoRoT-7b (Léger et al. 2009; Queloz et al. 2009) and GJ 1214b (Charbonneau et al. 2009). The former appears to be rocky (Léger et al. 2009), while the latter may contain significant amounts of water or a gaseous envelope (Rogers & Seager 2010). In order to address the ambiguities in the planet formation process, the radii of these planets must be measured

accurately and precisely. The *CoRoT* satellite already surpasses all other projects in the ability to make follow-up observations of CoRoT-7b (153 transits reported by Léger et al. 2009). The relatively recent detection and hence the dearth of follow-up measurements on GJ 1214b led us to focus on this object; a super-Earth planet orbiting an M dwarf star 13 pc from Earth (Charbonneau et al. 2009). The planetary nature of this transit has been confirmed by Sada et al. (2010).

The discovery of such a small-sized planet bodes well for transit searches for habitable planets around M dwarfs. The low luminosity of M dwarfs mean that their habitable zones are very close to the star (Kasting et al. 1993; Selsis et al. 2007). This increases the transit probability (Borucki & Summers 1984), and hence some of the first planets to be characterized as rocky and in the habitable zone may well be transiting planets around M dwarfs (Joshi et al. 1997). Although GJ 1214b most likely possesses a hydrogen-rich envelope, the detection of small planets such as this heralds the discovery of rocky habitable worlds beyond our solar system. M dwarfs make up a very large fraction of the stellar component of the Milky Way (Miller & Scalo 1979; Reid et al. 2002), so the prospect of habitable planets around M dwarfs raises the very interesting possibility that life-bearing planets may be fairly common in the galaxy. GJ 1214 may be a good target to search for a habitable zone planet. If the mutual inclination between GJ 1214b and a hypothetical habitable zone planet is small, the probability of detection is  $\sim 20\%$  (Gillon et al. 2011).

In this paper, we report observations of three transits of GJ 1214b, taken as part of the Apache Point Observatory Survey of Transit Light Curves of Exoplanets (APOSTLE). In Section 2, we outline our observations and data reduction techniques; in Section 3, we describe our light curve model and the use of Markov Chain Monte Carlo (MCMC) techniques to constrain system parameters from single and multi-wavelength data. In Section 4, we report the absence of strong transit timing variations (TTVs). In Section 5, we describe the derivation of various stellar and planetary parameters for the GJ 1214 system. In Section 6, we discuss the detection of a flare and a possible spot-crossing event. Finally, in Section 7 we summarize our findings.

<sup>1</sup> Virtual Planetary Laboratory, USA

## 2. DATA

### 2.1. APOSTLE Observations

We observed three transits of GJ 1214b on UT dates 2010 April 21, 2010 June 6, and 2010 July 6 using the ARC 3.5 m Telescope at Apache Point, New Mexico. All observations were made with *Agile*, a high-speed time-series CCD photometer based on the design of *Argos* (Nather & Mukadam 2004). *Agile* is a charge transfer CCD, that collects photons from the target at a 100% duty cycle. During transit observations the charge on *Agile* was read out at 45 s intervals using GPS-synchronized pulses with an absolute timing accuracy of less than a millisecond. Observations were made using *Agile*'s medium gain, slow readout mode with frames binned by a factor of two, yielding a plate-scale of  $0''.258 \text{ pixel}^{-1}$ . All APOSTLE light curves presented in this work were collected using the *r*-filter, which is similar to the Sloan Digital Sky Survey *r* filter (Fukugita et al. 1996).

During observations, we defocused the telescope to spread the stellar point-spread function (PSF) across multiple pixels in order to minimize systematics introduced by improper flat-fielding and to increase the integrated counts from the star. Count rate stability is affected by variable conditions during observing. We monitored the count rate and adjusted the telescope focus by small increments to raise or lower the maximum counts on the brightest star. By adjusting the focus we kept the maximum counts between 40k and 55k ADU. We did this because the instrument is known to show a nonlinear response at count levels greater than  $\sim 55\text{k}$ , and saturate at 61k counts. During stable conditions, these adjustments were made every 10 to 20 minutes while during poor conditions the adjustments were more frequent, at roughly five minute intervals. Less than 7% of frames on a given night were lost to saturation. For all our observations, the comparison star USNO-B1.0 0949–0280051 was the brightest object within *Agile*'s field of view,  $95''$  to the north of GJ 1214 (Monet et al. 2003). This object was brighter than GJ 1214 by a factor of 1.4 in the *r* band. It was also the only star brighter than GJ 1214 in *Agile*'s field of view, and hence was the only one used for differential photometry. On each night, we also collected twilight sky flats and dark frames (which were also used to correct for bias).

### 2.2. Image Reductions

We used a customized data reduction pipeline, written in interactive data language (IDL) to process *Agile* data. It performs standard image processing steps like dark subtraction and flat-fielding, but also implements nonlinearity corrections unique to *Agile*. The pipeline also creates an uncertainty map of the processed images by propagating pixel-to-pixel errors through each step of the reduction. In addition to the Poisson photon counting errors and read noise from the science images, the pipeline propagates the variance on the master dark and master flat during the reduction. Errors were also propagated for those pixels where the counts exceeded the nonlinearity threshold ( $\sim 55\text{k}$  counts) using the uncertainties in the empirically derived nonlinearity correction function. Typically 1%–5% of frames went above this threshold. The correction factor for counts on nonlinear pixels was typically 1.45% or less.

### 2.3. Photometry

We used SExtractor (Bertin & Arnouts 1996) to derive initial centroids of our defocused stars. Coordinates obtained from

SExtractor were then used for circular aperture photometry with the PHOT task in IRAF's NOAO.DIGIPHOT.APPHOT package. We derived flux estimates from a range of circular apertures with radii between 5 and 50 pixels, at intervals of 1 pixel. An outlier-rejected global median was used as the sky estimate. An optimal aperture was selected where the rms in the out-of-eclipse light curve was minimized. For GJ 1214 data, this aperture was typically 15–16 pixels in radius. This size was roughly four times the half-width at half-maximum of the PSFs. To derive photometric errors, we extracted counts from the error frames using the same centroids and apertures used for photometry on the target frames. Estimating photometric errors in this manner yielded uncertainties that were greater (by 50%) than the default errors reported by PHOT. It is useful to note that this method takes into account sources of error which are otherwise ignored by standard photometric techniques, e.g., fluctuations in the flat field and dark frame, and is thus more thorough. Photometric precision for our GJ1214 light curves was typically  $\sim 0.001 \text{ mag}$  from 45 s exposures.

### 2.4. Time Coordinates

The APOSTLE reduction pipeline converts time stamps from image headers to various commonly used time coordinates. To transform mid-exposure UTC (Coordinated Universal Time) stamps, we used a prescription similar to that used in the pulsar timing community (Seidelmann & Fukushima 1992; Standish 1998; Hobbs et al. 2006; Edwards et al. 2006). Recently, Eastman et al. (2010) recommended the use of Barycentric Dynamical Time (TDB) as the standard time coordinate for reporting ephemeris data derived from transit observations. All timing data presented in this work are in TDB. Comparisons of the APOSTLE pipeline's conversions with those produced by Eastman et al.'s (2010) freely available time coordinate converter show agreement at the microsecond level, which is safely below the levels of any experimental errors in our data.

### 2.5. Other Light Curves

The MEarth team graciously shared the light curves presented in Charbonneau et al. (2009), which were either from the array of MEarth ( $8 \times 40 \text{ cm}$ ) telescopes or *z*-filter observations from the Fred Lawrence Whipple Observatory's 1.2 m telescope (FLWO1.2m). We included these data in our multi-wavelength analysis of system parameters. We modified the time coordinate to  $\text{BJD}_{\text{TDB}}$ , and when data on nuisance parameters were available, we included them in our detrending analysis. Table 1 summarizes all light curves used in this work. We do not include several additional transits of GJ 1214b that have been reported recently, since they were released after the completion of our analysis (Sada et al. 2010; Carter et al. 2011; Berta et al. 2011).

## 3. SYSTEM PARAMETERS

### 3.1. Transit Light Curve Model and Detrending

APOSTLE transit light curves of GJ 1214b are shown in Figure 1. We use the light curve models described in Mandel & Agol (2002) assuming quadratic stellar limb darkening and a circular planetary orbit. Our transit code can fit for multiple transits simultaneously and allow for multiple sets of limb-darkening coefficients when data gathered using different filters are used. For the analysis presented in this paper, we used models which fit parameters in either one of the following two sets: for light curves from a single-filter, we used *Set 1*:

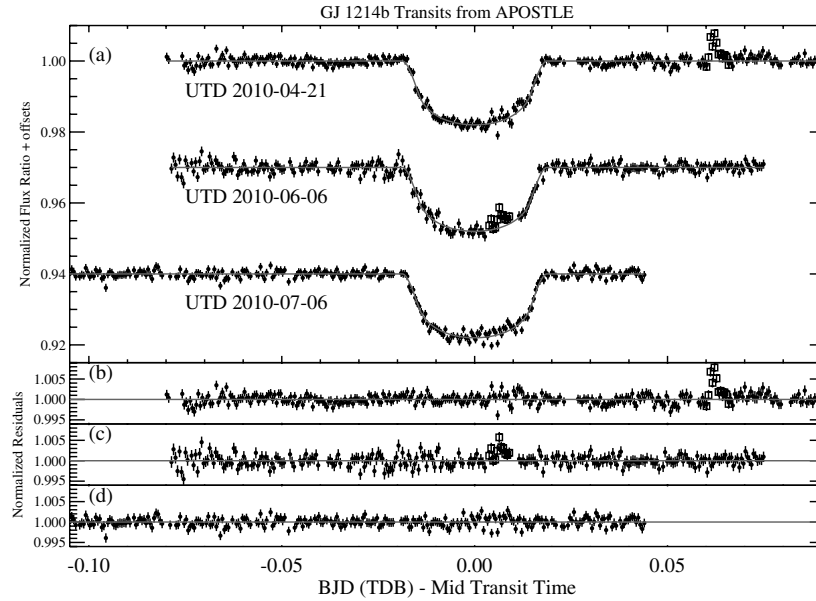


**Figure 1.** (a) Light curves of three transits of GJ 1214b observed by APOSTLE. The vertical axis shows the normalized flux ratio and the horizontal axis shows the time from mid-transit time in days. The transit time ( $T_0$ ) estimated for each transit was subtracted from the time stamp for each point. The solid circles represent the points used in the analysis, while the open squares represent the data that were excluded. The excluded data were either part of the stellar flare (UTD 2010 April 21) or the possible spot-crossing event (UTD 2010 June 6). The gray line shows the transit model. Panels (b), (c), and (d) show the light curves normalized by the transit model. The typical scatter in the normalized flux ratio (excluding the flare, spot, and transit signal) was  $\sim 0.0011$ .

**Table 1**  
Light Curve Data

Transit No.	Date	Data	Filter	Reference
1	UTD 2009 May 13	MEarth	...	Charbonneau et al. (2009)
2	UTD 2009 May 29	MEarth	...	Charbonneau et al. (2009)
3	UTD 2009 May 29	FLWO1.2m	$z$ band	Charbonneau et al. (2009)
4	UTD 2009 Jun 1	MEarth	...	Charbonneau et al. (2009)
5	UTD 2009 Jun 1	FLWO1.2m	$z$ band	Charbonneau et al. (2009)
6	UTD 2009 Jun 17	MEarth	...	Charbonneau et al. (2009)
7	UTD 2010 Apr 21	APOSTLE <sup>a</sup>	$r$ band	This work
8	UTD 2010 Jun 6	APOSTLE <sup>a</sup>	$r$ band	This work
9	UTD 2010 Jul 6	APOSTLE <sup>a</sup>	$r$ band	This work

**Note.** <sup>a</sup> Entire light curves for APOSTLE are provided with the online version. See also Table 6.

$\theta_1 = \{t_T, t_G, D, v_1, v_2, T_{i...N_T}\}$  and for the joint analysis of light curves gathered at different wavelengths, we used *Set 2*:  $\theta_2 = \{t_T, t_G, R_p^2/R_\star^2, v_{1,j...N_F}, v_{2,j...N_F}, T_{i...N_T}\}$ , with the parameters described as follows

The parameters  $t_T$  and  $t_G$  are approximately the transit duration and ingress/egress duration, respectively (same as  $T$  and  $\tau$  from Carter et al. 2008). The transit duration is defined as the time between the middle of ingress and the middle of egress. The ingress duration describes the time between the start of the eclipse till the planet has completely crossed the limb of the star. The duration of egress is assumed to be the same. In the limit of circular orbits,  $R_p \ll R_\star$  and  $R_\star \ll a$ , these two parameters can be approximated as

$$t_T = 2 \frac{R_\star}{v} \sqrt{1 - b^2} \quad (1)$$

$$t_G = 2 \frac{R_p}{v \sqrt{1 - b^2}}, \quad (2)$$

where the orbital speed  $v = 2\pi a/P$  and the impact parameter  $b = a \sin i/R_\star$ . The terms  $a$ ,  $P$ ,  $i$ ,  $R_p$ , and  $R_\star$  are the semimajor axis, orbital period, inclination, planetary radius, and stellar radius, respectively (Carter et al. 2008).

We assume quadratic limb darkening as described in Mandel & Agol (2002), and assume the transit depth approximately changes as

$$D(b) = \frac{R_p^2}{R_\star^2} \frac{(1 - \gamma_1(1 - \sqrt{1 - b^2}) - \gamma_2(1 - \sqrt{1 - b^2})^2)}{(1 - \frac{\gamma_1}{3} - \frac{\gamma_2}{6})}, \quad (3)$$

where  $\gamma_1$  and  $\gamma_2$  are the quadratic limb-darkening coefficients from Mandel & Agol (2002) and  $R_p^2/R_\star^2$  is the square of the planet-to-star radius ratio. Solving for the impact parameter in Equations (1) and (2) gives  $b = \sqrt{1 - (t_T/t_G)(R_p/R_\star)}$ . So given  $t_T$ ,  $t_G$ ,  $D(b)$ , and the limb-darkening coefficients, the ratio  $R_p/R_\star$  can be determined by solving a sextic equation in  $(R_p/R_\star)^{1/2}$ . The difference between the two fit parameter sets ( $\theta_1$  and  $\theta_2$ ) are the variables  $D$  and  $R_p^2/R_\star^2$ . Since the limb-darkening coefficients are dependent on the waveband used for observations,  $R_p^2/R_\star^2$  is commonly used to fit for the depth of transit light curves, but  $D$  might be better suited for constraining the transit depth of single-filter data, especially when the star is expected to be strongly limb darkened.

The terms  $v_1$  and  $v_2$  are linear combinations of the quadratic limb-darkening coefficients,  $v_1 = \gamma_1 + \gamma_2$  and  $v_2 = \gamma_1 - \gamma_2$ . These linear combinations were used since it is known that

directly fitting for limb-darkening coefficients results in strongly anticorrelated error distributions for transit parameters (Brown et al. 2001). In order to avoid unphysical limb-darkening profiles, we applied the bounds  $v_1 + v_2 > 0$  and  $0 < v_1 < 1$ . The  $T_i$  terms are the times of transit center. The subscripts  $i \dots N_T$  and  $j \dots N_F$  are used to denote multiple transits ( $N_T$ ) and multiple filters ( $N_F$ ), respectively. The corresponding transit numbers ( $i \dots N_T$ ) are listed in Table 1. Together, these parameters define the model transit light curve.

There are many systematic trends that may be introduced over the course of observing that may not be accounted for by the reduction protocol described in Section 2.2, for example, differential extinction due to air-mass variation or photometric variation due to centroids wandering over pixels of varying sensitivities on an imperfectly flat-fielded image. So for each image, we extracted a set of nuisance parameters which were then used to compute a correction function (i.e., detrending function) to remove these trends. We modeled the correction function as a linear combination of nuisance parameters

$$F_{\text{cor},i} = a_0 + \sum_{k=1}^{N_{\text{nus}}} a_k X_{k,i}, \quad (4)$$

where  $X_{k,i}$  are the nuisance parameters and  $a_{k,i}$  are the corresponding coefficients. A typical set of nuisance parameters included (1) the air mass, (2) the centroid positions of the target and reference stars, (3) the local sky around the target and comparison stars, (4) the global sky, and (5) the total counts in the area that defined the photometric aperture on the master dark and (6) the master sky flat.

For each night, the entire light curve is normalized to one by an initial best-fit transit model. Then we fit for the coefficients  $a_k$  of the correction functions using these model-normalized light curves and a generalized linear least squares minimizer. The  $a_0$  term is set to a constant, which in this case is one because of the way the light curve is normalized. We found that the most significant systematic trends in the model-normalized light curves were correlated with air mass and the counts on the master flat. This tells us that differential extinction and imperfect flat-fielding are the two greatest sources of systematic effects.

Once the correction function and the model are derived, we compute the goodness of fit to our data as

$$\chi^2 = \sum_i^{N_{\text{Data}}} \frac{(O_i - M_i(\theta) - F_{\text{cor},i})^2}{\sigma_i^2}, \quad (5)$$

where the  $O_i$  and  $\sigma_i$  are the observed data and associated errors,  $M_i$  is the transit model, and  $F_{\text{cor},i}$  is the detrending function. For all subsequent optimization with either Markov chains or a nonlinear minimizer, Equation (5) is used to evaluate the goodness of fit. One must note that we devised routines such that the correction function is recomputed along with the model light curve for each step in the Markov chain or each iteration in the nonlinear minimizer.

In Section 6, we note the possible evidence for stellar activity in some of our light curves. These features were seen in light curves after reductions and detrending, and we believe that they are not associated with any systematic effects in the data. We excluded these points from our analysis of system parameters.

### 3.2. Markov Chain Monte Carlo

Bayesian inference techniques like MCMC have become a popular tool for constraining system parameters from observa-

tional data. We used the Metropolis–Hastings (M-H) algorithm, a well-known MCMC method, to constrain the uncertainties for fitted parameters in our transit model. Tegmark et al. (2004) and Ford (2005) have very good descriptions of the algorithm and its application to relevant astronomical data. Our prescription is closest to that described by Ford (2005). We approximate the posterior distribution and joint probability distribution of our model parameters given the observed data  $\mathbf{O}$ , as  $P(\theta | \mathbf{O}) \propto P(\theta)P(\mathbf{O} | \theta) \propto e^{-\chi(\theta)^2/2}$ . Our MCMC routines use the standard stepping and selection rules of the M-H algorithm. The jump functions for our parameters are of the form

$$\theta_{j+1} = \theta_j + G(0, \sigma_\theta^2) f, \quad (6)$$

where  $\theta$  and  $\sigma_\theta$  are the vectors of model parameters and their associated step-sizes, respectively, and  $G(0, \sigma_\theta^2)$  is a random number drawn from a normal distribution with a mean of 0 and a variance of  $\sigma_\theta^2$ . The factor  $f$  is an adaptive step-size controller which is used to guide the chain to the optimal acceptance rate. For the case where a jump is performed for the entire vector of model parameters, it has been shown that the optimal acceptance rate is  $\sim 23\%$  (Gelman et al. 2003). This desired rate is achieved by adjusting the step-size controller ( $f$ ) every 100 accepted steps according to  $f_{\text{new}} = 434 f_{\text{old}}/N_{\text{trials}}$ , where  $N_{\text{trials}}$  are the number of steps attempted for the last 100 accepted steps (see also Collier Cameron et al. 2007).

By varying the entire vector of model parameters and applying a single step-size modifier, we run the risk of using mismatched step-sizes and undersampling posterior distributions. Statisticians have shown that well-constructed chains will properly sample posterior distributions given the correct acceptance rate (Gelman et al. 2003). However, the acceptance rate is guided by the location of the chain in parameter space, as steps in low-probability (large  $\chi^2$ ) regions of parameter space are accepted less often than those in high-probability regions. The key to a well-constructed chain is to choose the relative starting step-sizes, for the parameter ensemble, such that they *all* roam high- and low-probability regions of parameter space at roughly the same rate. To find such a set of step-sizes, we ran a set of exploratory chains (40,000 iterations), stepping only one parameter at a time, until the step-size controller settled the simulation to an acceptance rate of  $\sim 44\%$  (the optimal acceptance rate for the one-dimensional case, Gelman et al. 2003). Most of the chains reached this acceptance rate at an iteration between  $\sim 1000$  and 7000. The jumps made near the end of these exploratory chains proved to be good choices for the starting step-sizes of the longer, multi-parameter MCMC runs.

We ran 10 long MCMC chains for different combinations of parameter sets and light curves. Table 2 lists the names of the chains, the corresponding light curve data, the parameter sets used and some statistics from our post-run analysis of the chains. The chains are numbered from 001 to 005 which represent the five different data sets used—listed in Column 2. Chains 001, 004, and 005 are single-filter data sets corresponding to APOSTLE, MEarth, and FLWO1.2m observations, respectively. These were used to test the models where the transit depth  $D$  was fit, for the highly limb-darkened case (see Section 3.1). Chain 002 was simply a redo of Charbonneau et al.’s (2009) analysis with our transit model and MCMC framework. In chain 003, we fit for transit parameters using all three data sets. The tags “a” and “b” denote whether the limb-darkening coefficients were left fixed or open, respectively. For chains where the limb-darkening parameters were fixed (“a”), we either chose values

**Table 2**  
MCMC Analysis

Chain Name	Data Set	Model Parameter Set	$N_{\text{pars}}$	Chain Length	Correlation Length	Effective Length	$\chi^2$	dof
001a	APOSTLE	$\theta_1$	6	999,820	12	83,318	674	808
001b	APOSTLE	$\theta_1$	8	1,196,226	283	3774	673	806
002a	MEarth + FLWO1.2m	$\theta_2$	9	998,308	66	15,126	1279	1294
002b	MEarth + FLWO1.2m	$\theta_2$	13	1,193,569	939	1271	1249	1290
003a	APOSTLE + MEarth + FLWO1.2m	$\theta_2$	12	997,202	84	11,871	2067	2105
003b	APOSTLE + MEarth + FLWO1.2m	$\theta_2$	18	2,398,779	3299	727	1947	2099
004a	MEarth	$\theta_1$	7	998,975	16	62,436	1036	813
004b	MEarth	$\theta_1$	9	1,195,920	199	4080	994	811
005a	FLWO1.2m	$\theta_1$	5	976,447	8	122,056	484	478
005b	FLWO1.2m	$\theta_1$	7	1,198,883	118	10,160	479	476

from the literature or used values which were found to be suitable by others. For the APOSTLE  $r$ -band data set, we chose values from Claret (2004) for a 3000 K star:  $(v_{1,\text{APOSTLE}}, v_{2,\text{APOSTLE}}) = (0.908, 0.305)$ . For the MEarth and FLWO1.2m data, we used unpublished values used by Charbonneau et al. (2009) in their fit (P. Nutzman 2010, private communication). For the MEarth “filter” we used  $(v_{1,\text{MEarth}}, v_{2,\text{MEarth}}) = (0.145, 0.639)$  and for the FLWO1.2  $z$ -band filter we used  $(v_{1,\text{FLWO1.2m}}, v_{2,\text{FLWO1.2m}}) = (0.404, -0.289)$ . Since it is well known that these parameters are highly degenerate, the “b” chains were run as a test of how well these light curves could be used to constrain stellar limb darkening.

The number of iterations used for long MCMC chains were  $1 \times 10^6$  for all “a” chains and  $1.2 \times 10^6$  for all “b” chains, except chain 003b. For 003b, we ran the chain for  $2.5 \times 10^6$  iterations. These computations took a total of 80 CPU hours to complete on Linux workstations. For each chain, we discarded the initial phase where the acceptance rate was not close to the optimal rate. We selected the steps once the chains stabilized (i.e., approached within 5% of the optimal acceptance rate). The number of selected steps are listed in Table 2 under the “Chain Length” column.

The M-H algorithm’s jump function is only dependent on the previous location of a step in the chain, so it is not unusual for sequential points in the chain to be correlated. The dimensionless autocorrelation function provides a good assessment of how many independent points there are in a chain. We computed this for each open parameter per chain, using the prescription of Tegmark et al. (2004), and derived the correlation and effective lengths for each chain (Table 2). The effective length (the chain length divided by the correlation length) is a measure of the number of independent points in a chain and must be large ( $\gg 1$ ) for the errors derived from a chain to be meaningful. A large number of independent points defines a statistically significant, well-sampled posterior distribution. We found that chains where the limb darkening was fixed (“a” chains) had greater effective lengths when compared to chains where limb-darkening parameters were left open (“b” chains). Chain 003b had the lowest effective length since it had the largest number of open parameters (including three pairs of limb-darkening parameters) and was plagued with degeneracies between various parameters.

### 3.3. Parameters and Errors

System parameters derived from our analysis are presented in Tables 3 and 4 for the single and multi-wavelength data sets, respectively. Directly fit model parameters are listed in the

table subsection titled “Model” and correspond to the variables described in Section 3.1 as part of  $\theta_1$  and  $\theta_2$ . The values listed in the tables were obtained using the minimization package MINUIT (James et al. 1994). The  $\chi^2$  from the best-fit model and the degrees of freedom (dof) are listed in the last two columns of Table 2. The ensemble of points from the posterior distributions of “Model” parameters were then used to compute posterior distributions of various “Derived” parameters (Seager & Mallén-Ornelas 2003; Carter et al. 2008). We chose to present the following seven derived quantities: (1) the planet-to-star radius ratio ( $R_p/R_*$ ), (2) the orbital period, (3) the impact parameter ( $b$ ), (4) semimajor axis in stellar radius units ( $a/R_*$ ), (5) orbital inclination ( $i$ ), (6) orbital velocity ( $v/R_*$ ) normalized by stellar radius, and (7) the stellar density ( $\rho_*$ ). The errors for both the “Model” and “Derived” parameters were then computed by sorting these data and choosing the 68.3% confidence intervals to represent the  $1\sigma$  uncertainties. For cases where the parameter values were distributed asymmetrically around the best-fit value (at a level  $> 10\%$ ), we present upper and lower uncertainty estimates.

Figure 2 shows the joint probability distributions of directly fit model parameters from chain001a with the crosshairs marking the best-fit values. The distributions of “Model” parameters shown in Figure 2 show little or no mutual correlations, while some parameters from the “Derived” (Figure 3) ensemble show strong degeneracies. It is fairly common practice to use some of the parameters listed here as “Derived” as the directly fit model parameters (e.g., Holman et al. 2006; Winn et al. 2007; Collier Cameron et al. 2007). Using MCMC to obtain error estimates on such a parameter set is challenging since these degeneracies can result in (1) chains that have short effective lengths (slow convergence) or (2) incomplete sampling of posterior probability distributions. Both problems could be reduced by running longer chains. However, this solution is not always practical as the number of required steps may be prohibitively large or unknown. The lack of degeneracies in the “Model” parameters is a result of choosing a set of nearly orthogonal parameters, as described in Section 3.1.

Figure 4 shows our results from chain001b. This chain is similar to chain001a, except that the limb-darkening parameters  $v_1$  and  $v_2$  are free parameters in this case (but within bounds as mentioned in Section 3.1). We note that correlations appear between the limb-darkening parameters (Figure 4 panel— $v_{1,\text{APOSTLE}}$  VERSUS  $v_{2,\text{APOSTLE}}$ ) and other parameters which previously (in “chain001a”) showed uncorrelated distributions. The most strongly affected are the parameters  $t_T$ ,  $t_G$ , and  $D$ . The degeneracy between the ingress/egress duration ( $t_G$ ) and the limb-darkening parameters can be understood simply by the fact that they both affect the overall shape of the light curve.

**Table 3**  
Parameter Set  $\theta_1$ 

Parameter/Chain	001a	001b	004a	004b	005a	005b	Charbonneau et al. (2009) <sup>a</sup>	Units
	Model							
D	0.0179 <sup>+0.0001</sup> <sub>-0.0002</sub>	0.0179 <sup>+0.0002</sup> <sub>-0.0001</sub>	0.0141 <sup>+0.0015</sup> <sub>-0.0012</sub>	0.0172 <sup>+0.0009</sup> <sub>-0.0013</sub>	0.0157 <sup>+0.0003</sup> <sub>-0.0002</sub>	0.0161 <sup>+0.0004</sup> <sub>-0.0003</sub>	0.0135 ± 0.0002	...
$t_T$	0.0326 <sup>+0.0001</sup> <sub>-0.0002</sub>	0.0329 <sup>+0.0001</sup> <sub>-0.0010</sub>	0.0311 ± 0.0001	0.0314 ± 0.0002	0.0314 <sup>+0.0002</sup> <sub>-0.0003</sub>	0.0322 <sup>+0.0003</sup> <sub>-0.0009</sub>	0.0321 ± 0.1529	day
$t_G$	0.0046 ± 0.0004	0.0041 ± 0.0007	0.0037 <sup>+0.0009</sup> <sub>-0.0001</sub>	0.0039 <sup>+0.0006</sup> <sub>-0.0001</sub>	0.0053 <sup>+0.0008</sup> <sub>-0.0004</sub>	0.0042 <sup>+0.0012</sup> <sub>-0.0001</sub>	0.0043 ± 0.0203	day
$v1_{\text{APOSTLE}}$	(0.908)	0.97 <sup>+0.03</sup> <sub>-0.30</sub>	...	...	...	...	...	...
$v2_{\text{APOSTLE}}$	(0.305)	0.38 <sup>+0.64</sup> <sub>-0.02</sub>	...	...	...	...	...	...
$v1_{\text{MEarth}}$	...	...	(0.145)	0.29 <sup>+0.13</sup> <sub>-0.15</sub>	...	...	(0.145)	...
$v2_{\text{MEarth}}$	...	...	(0.639)	1.15 <sup>+0.64</sup> <sub>-0.30</sub>	...	...	(0.639)	...
$v1_{\text{FLWO1.2m}}$	...	...	...	...	(0.404)	0.63 <sup>+0.11</sup> <sub>-0.38</sub>	(0.404)	...
$v2_{\text{FLWO1.2m}}$	...	...	...	...	(-0.289)	0.03 <sup>+1.21</sup> <sub>-0.30</sub>	(-0.289)	...
$T_1$ 2454964+	...	...	0.944600 ± 0.000794	0.944746 ± 0.000792	...	...	0.944959 ± 0.000403	BJD <sub>TDB</sub>
$T_2$ 2454980+	...	...	0.748725 ± 0.000272	0.748758 ± 0.000271	...	...	0.748719 ± 0.000090	BJD <sub>TDB</sub>
$T_3$ 2454980+	...	...	...	...	0.748727 ± 0.000469	0.748712 ± 0.000469	...	BJD <sub>TDB</sub>
$T_4$ 2454983+	...	...	0.909475 ± 0.000233	0.909546 ± 0.000233	...	...	0.909509 ± 0.000090	BJD <sub>TDB</sub>
$T_5$ 2454983+	...	...	...	...	0.909534 ± 0.000446	0.909542 ± 0.000446	...	BJD <sub>TDB</sub>
$T_6$ 2454999+	...	...	0.713429 ± 0.000260	0.713418 ± 0.000260	...	...	0.713450 ± 0.000126	BJD <sub>TDB</sub>
$T_7$ 2455307+	0.892592 ± 0.000277	0.892584 ± 0.000278	...	...	...	...	...	BJD <sub>TDB</sub>
$T_8$ 2455353+	0.724451 ± 0.000318	0.724476 ± 0.000319	...	...	...	...	...	BJD <sub>TDB</sub>
$T_9$ 2455383+	0.752124 ± 0.000266	0.752124 ± 0.000266	...	...	...	...	...	BJD <sub>TDB</sub>
	Derived							
$R_p/R_*$	0.1041 <sup>+0.0027</sup> <sub>-0.0024</sub>	0.0846 <sup>+0.0267</sup> <sub>-0.0150</sub>	0.1092 <sup>+0.0082</sup> <sub>-0.0050</sub>	0.1011 <sup>+0.0116</sup> <sub>-0.0057</sub>	0.1173 <sup>+0.0019</sup> <sub>-0.0011</sub>	0.1038 <sup>+0.0140</sup> <sub>-0.0023</sub>	0.1162 ± 0.0007	...
P(1.5804 days+)	0.61 ± 0.25	0.65 ± 0.25	0.10 ± 1.38	... 0.40 ± 1.40	0.31 ± 9.99	0.52 ± 9.94	... 0.65 ± 1.01	s
b	0.51 ± 0.04	0.52 <sup>+0.04</sup> <sub>-0.07</sub>	0.28 <sup>+0.18</sup> <sub>-0.02</sub>	0.44 <sup>+0.03</sup> <sub>-0.10</sub>	0.55 <sup>+0.07</sup> <sub>-0.05</sub>	0.51 <sup>+0.06</sup> <sub>-0.12</sub>	0.35 <sup>+0.06</sup> <sub>-0.08</sub>	...
$a/R_*$	13.28 ± 0.40	13.06 <sup>+0.71</sup> <sub>-0.12</sub>	15.53 <sup>+0.10</sup> <sub>-1.11</sub>	14.31 <sup>+0.69</sup> <sub>-0.20</sub>	13.42 <sup>+0.45</sup> <sub>-0.81</sub>	13.55 <sup>+0.82</sup> <sub>-0.47</sub>	14.66 ± 0.41	...
i	87.80 ± 0.26	87.73 <sup>+0.39</sup> <sub>-0.21</sub>	88.95 <sup>+0.07</sup> <sub>-0.81</sub>	88.22 <sup>+0.48</sup> <sub>-0.15</sub>	87.66 <sup>+0.27</sup> <sub>-0.48</sub>	87.84 <sup>+0.58</sup> <sub>-0.32</sub>	88.62 <sup>+0.35</sup> <sub>-0.28</sub>	deg
$v/R_*$	52.80 ± 1.58	51.91 <sup>+2.81</sup> <sub>-0.48</sub>	61.73 <sup>+0.42</sup> <sub>-4.42</sub>	56.88 <sup>+2.76</sup> <sub>-0.78</sub>	53.34 <sup>+1.79</sup> <sub>-3.21</sub>	53.88 <sup>+3.24</sup> <sub>-1.85</sub>	58.28 ± 1.63	day <sup>-1</sup>
$\rho_*$	17.75 ± 1.60	16.86 <sup>+2.89</sup> <sub>-0.47</sub>	28.36 <sup>+0.58</sup> <sub>-5.67</sub>	22.18 <sup>+3.39</sup> <sub>-0.90</sub>	18.29 <sup>+1.91</sup> <sub>-3.10</sub>	18.86 <sup>+3.62</sup> <sub>-1.88</sub>	23.90 ± 2.10	g cm <sup>-3</sup>

**Note.** <sup>a</sup> For those parameters not explicitly listed by Charbonneau et al. (2009; e.g.,  $t_T$  and  $t_G$ ) we computed them using the expressions in Carter et al. (2008) and propagated the errors assuming that they had Gaussian distributions. The values shown within parentheses were held fixed.

**Table 4**  
Parameter Set  $\theta_2$ 

Parameter/Chain	002a	002b	003a	003b	Charbonneau et al. (2009) <sup>a</sup>	Units
Model						
$R_p^2/R_\star^2$	$0.0145 \pm 0.0002$	$0.0137^{+0.0007}_{-0.0002}$	$0.0143^{+0.0002}_{-0.0001}$	$0.0133^{+0.0006}_{-0.0001}$	$0.0135 \pm 0.0002$	...
$t_T$	$0.0310^{+0.0001}_{-0.0002}$	$0.0316^{+0.0002}_{-0.0004}$	$0.0316 \pm 0.0001$	$0.0321^{+0.0002}_{-0.0004}$	$0.0321 \pm 0.1529$	day
$t_G$	$0.0045^{+0.0005}_{-0.0003}$	$0.0041^{+0.0006}_{-0.0002}$	$0.0045^{+0.0002}_{-0.0001}$	$0.0037 \pm 0.0002$	$0.0043 \pm 0.0203$	day
$v1_{\text{APOSTLE}}$	...	...	(0.908)	$0.71^{+0.14}_{-0.08}$	...	...
$v2_{\text{APOSTLE}}$	...	...	(0.305)	$1.01^{+0.20}_{-0.43}$	...	...
$v1_{\text{MEarth}}$	(0.145)	$0.38^{+0.08}_{-0.21}$	(0.145)	$0.53^{+0.11}_{-0.21}$	(0.145)	...
$v2_{\text{MEarth}}$	(0.639)	$1.05^{+0.72}_{-0.31}$	(0.639)	$0.47^{+0.68}_{-0.28}$	(0.639)	...
$v1_{\text{FLWO1.2m}}$	(0.404)	$0.45^{+0.15}_{-0.19}$	(0.404)	$0.61^{+0.13}_{-0.20}$	(0.404)	...
$v2_{\text{FLWO1.2m}}$	(-0.289)	$0.55 \pm 0.58$	(-0.289)	$0.24 \pm 0.51$	(-0.289)	...
$T_1$ 2454964+	$0.944759 \pm 0.000794$	$0.944757 \pm 0.000789$	$0.944779 \pm 0.000799$	$0.944752 \pm 0.000788$	$0.944959 \pm 0.000403$	BJD <sub>TDB</sub>
$T_2$ 2454980+	$0.748738 \pm 0.000266$	$0.748755 \pm 0.000267$	$0.748721 \pm 0.000263$	$0.748793 \pm 0.000264$	$0.748719 \pm 0.000090$	BJD <sub>TDB</sub>
$T_3$ 2454980+	$0.748754 \pm 0.000380$	$0.748713 \pm 0.000414$	$0.748740 \pm 0.000390$	$0.748758 \pm 0.000417$	...	BJD <sub>TDB</sub>
$T_4$ 2454983+	$0.909481 \pm 0.000229$	$0.909467 \pm 0.000230$	$0.909490 \pm 0.000228$	$0.909506 \pm 0.000228$	$0.909509 \pm 0.000090$	BJD <sub>TDB</sub>
$T_5$ 2454983+	$0.909551 \pm 0.000373$	$0.909532 \pm 0.000400$	$0.909552 \pm 0.000381$	$0.909502 \pm 0.000401$	...	BJD <sub>TDB</sub>
$T_6$ 2454999+	$0.713464 \pm 0.000256$	$0.713491 \pm 0.000257$	$0.713442 \pm 0.000253$	$0.713506 \pm 0.000253$	$0.713450 \pm 0.000126$	BJD <sub>TDB</sub>
$T_7$ 2455307+	...	...	$0.892454 \pm 0.000271$	$0.892501 \pm 0.000263$	...	BJD <sub>TDB</sub>
$T_8$ 2455353+	...	...	$0.724539 \pm 0.000307$	$0.724462 \pm 0.000311$	...	BJD <sub>TDB</sub>
$T_9$ 2455383+	...	...	$0.752143 \pm 0.000260$	$0.752144 \pm 0.000264$	...	BJD <sub>TDB</sub>
Derived						
$R_p/R_\star$	$0.1203^{+0.0009}_{-0.0006}$	$0.1171^{+0.0029}_{-0.0008}$	$0.1195^{+0.0008}_{-0.0004}$	$0.1152^{+0.0026}_{-0.0003}$	$0.1162 \pm 0.0007$	...
$P(1.5804 \text{ days}+)$	... $0.39 \pm 1.38$	... $0.27 \pm 1.42$	$0.47 \pm 0.04$	$0.46 \pm 0.04$	... $0.65 \pm 1.01$	sec
$b$	$0.42^{+0.08}_{-0.07}$	$0.32^{+0.13}_{-0.07}$	$0.41^{+0.04}_{-0.03}$	$0.09^{+0.24}_{-0.04}$	$0.35^{+0.06}_{-0.08}$	...
$a/R_\star$	$14.70^{+0.49}_{-0.67}$	$15.08^{+0.30}_{-0.74}$	$14.54^{+0.19}_{-0.33}$	$15.60^{+0.08}_{-0.72}$	$14.66 \pm 0.41$	...
$i$	$88.36^{+0.34}_{-0.42}$	$88.79^{+0.29}_{-0.58}$	$88.39^{+0.14}_{-0.21}$	$89.67^{+0.15}_{-0.94}$	$88.62^{+0.35}_{-0.28}$	deg
$v/R_\star$	$58.46^{+1.96}_{-2.66}$	$59.94^{+1.19}_{-2.95}$	$57.81^{+0.75}_{-1.32}$	$62.02^{+0.33}_{-2.87}$	$58.28 \pm 1.63$	day <sup>-1</sup>
$\rho_\star$	$24.09^{+2.50}_{-3.14}$	$25.97^{+1.58}_{-3.65}$	$23.29^{+0.92}_{-1.55}$	$28.76^{+0.45}_{-3.82}$	$23.90 \pm 2.10$	g cm <sup>-3</sup>

**Note.** <sup>a</sup> For those parameters not explicitly listed by Charbonneau et al. (2009; e.g.,  $t_T$  and  $t_G$ ) we computed them using the expressions in Carter et al. (2008) and propagated the errors assuming that they had Gaussian distributions. The values shown within parentheses were held fixed.

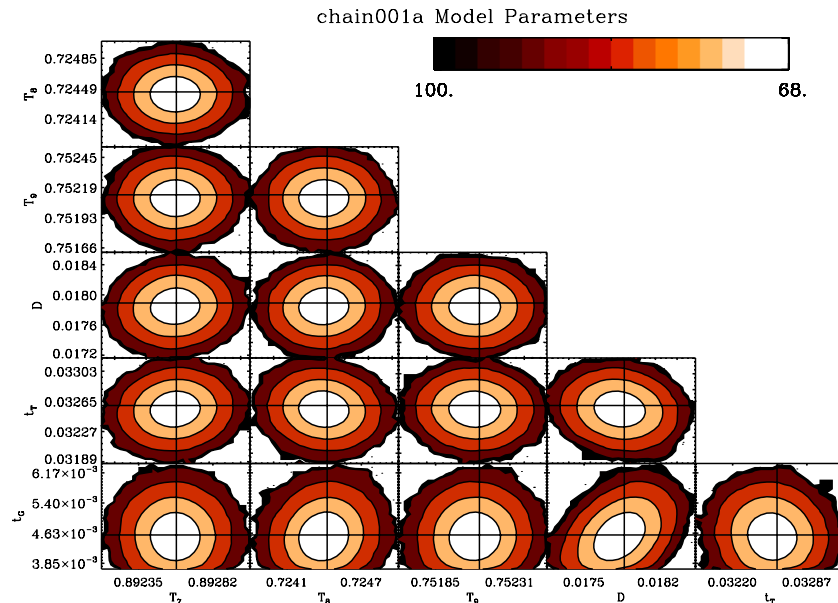


**Figure 2.** Joint probability distributions for all fitted transit “Model” parameters fit in MCMC chain001a. The model parameters were fit to APOSTLE light curves using the parameter set  $\theta_1$ . The numbers and units correspond to those listed in Table 3. The solid line crosshairs mark the location of the best-fit values (also from Table 3). The contours mark the  $1\sigma$ ,  $2\sigma$ ,  $3\sigma$ ,  $4\sigma$ , and  $5\sigma$  regions, each enclosing 68.27%, 95.45%, 99.73%, 99.994%, and 99.99994% of the points in the distributions, respectively.

(A color version of this figure is available in the online journal.)

Limb darkening can change the profile of the ingress and egress regions of the light curve, while  $t_G$  determines the start and end points of ingress and egress. So, given the error bars and scatter

in our data points, a range of limb darkening and  $t_G$  values can produce good fits. Our inability to constrain these parameters simultaneously seems to suggest that millimagnitude photometry

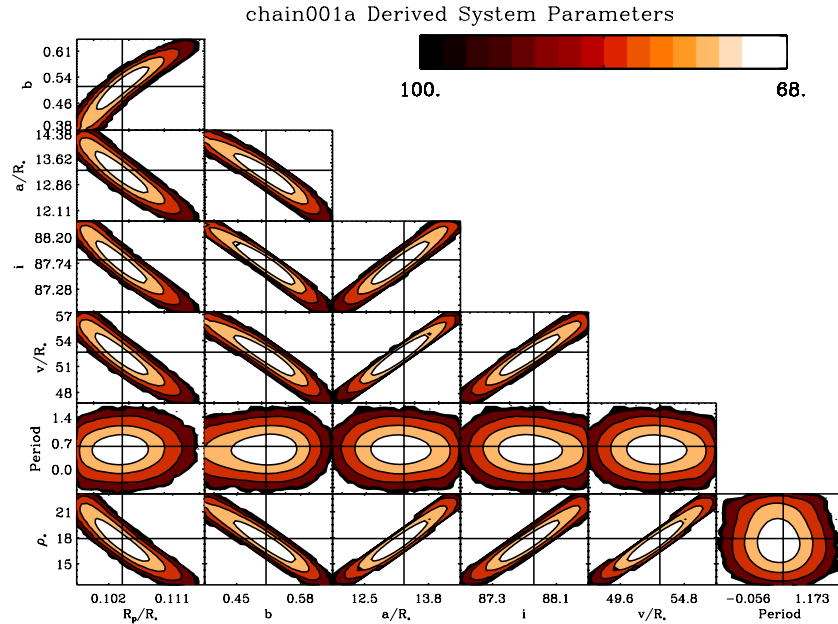


**Figure 3.** Joint probability distributions for all “Derived” parameters fit in MCMC chain001a. The numbers and units correspond to those listed in Table 3. The solid line crosshairs mark the location of the best-fit values (also from Table 3). The contours and color scheme are the same as what is shown in Figure 2. Several parameters have strong mutual correlations.

(A color version of this figure is available in the online journal.)

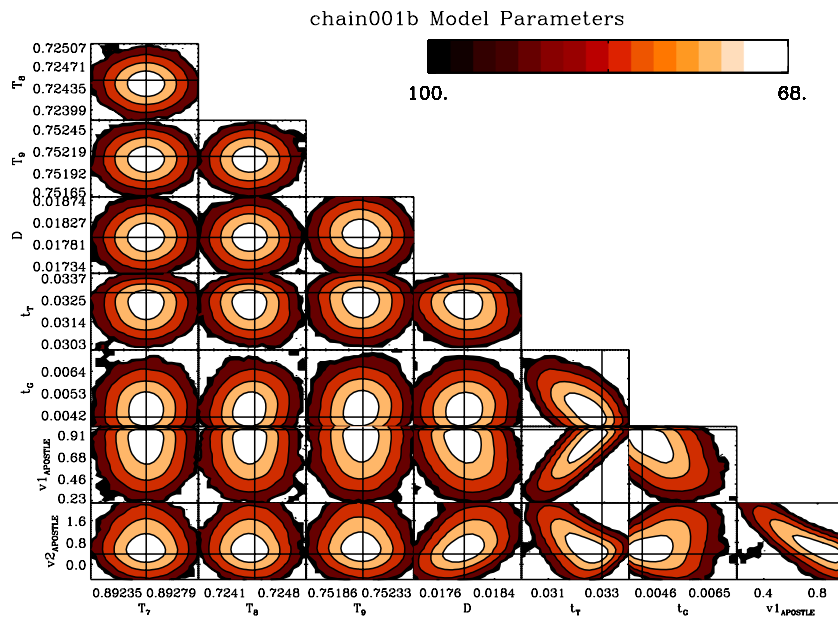


**Figure 4.** Joint probability distributions for all transit model parameters fit in MCMC chain001b. The model parameters were fit to APOSTLE light curves using the parameter set  $\theta_1$ . The numbers and units correspond to those listed in Table 3. The solid line crosshairs mark the location of the best-fit values (also from Table 3). The contours and color scheme are the same as what is shown in Figure 2. This set is different from chain001a, as the limb-darkening parameters  $v1_{\text{APOSTLE}}$  and  $v2_{\text{APOSTLE}}$  were varied in this analysis. There are strong correlations seen between various model parameters (e.g.,  $D$  vs.  $t_T$  and  $t_T$  vs.  $v1_{\text{APOSTLE}}$ ). We can also see how the nonlinear minimizer converges to a low value for  $t_G$  and a high value for  $t_T$ . This seems to be a result of a degeneracy with the open  $v1_{\text{APOSTLE}}$  parameter.

(A color version of this figure is available in the online journal.)

might not be sufficient for the complete characterization of transit light curves. Southworth (2008) have noted this before and state that high-precision space-based data may be needed to constrain limb darkening from transits (e.g., Pont et al. 2007; *Hubble Space Telescope* data). Degeneracies introduced by limb darkening resulted in best-fit parameters that were discrepant for the “b” chains (Tables 3 and 4), while those from the “a” chains were more or less consistent with each other. We conclude that results from the “b” chains were unreliable, so we elect to dis-

cuss results in which the limb-darkening parameters are held fixed.

### 3.3.1. Which Parameter Set to Consider?

We analyzed a combination of five different data sets and two parameter options (chains “a” and “b,” see Table 2). Out of the five “a” chains, three chains, 001a, 004a, and 005a, were single filter data sets (see Table 3). These serve as simple checks on

our transit model and MCMC framework. They also highlight the use of the maximum transit depth ( $D$ ) instead of the square of planet-to-star radius ratio ( $R_p^2/R_\star^2$ ) for single filter data. We find that  $D$  has weaker covariance with  $t_G$  and  $t_T$  than does  $R_p^2/R_\star^2$ . Due to the small number of light curves for each of these three sets, we see not surprisingly that parameters like  $R_p/R_\star$  and the period are constrained to poorer precision. The 002 chains were simply a redo of Charbonneau et al.’s (2009) analysis with our transit model and MCMC framework. We find that the results are in good agreement with Charbonneau et al.’s (2009) findings. The largest parameter and data set presented in this work is chain003a and represent the joint analysis of the multi-wavelength data set listed in Table 1 using our transit model framework. The findings are in good agreement with the results presented in Charbonneau et al. (2009). From Table 2, we can safely say that the MCMC analysis for this chain is quite reliable. Thus, the results from chain003a are the best to consider from this work and are used in the discussions that follow.

#### 4. TRANSIT TIMING VARIATIONS

At the time of submitting this paper, 10 transits were reported for GJ 1214b (including Charbonneau et al. 2009; Sada et al. 2010). Transit times reported in Charbonneau et al. (2009) and Sada et al. (2010) were in HJD<sub>UTC</sub>, i.e., JD representation of UTC corrected for the light travel time delay to the solar system barycenter. These were converted to BJD<sub>TDB</sub>. For the transits observed by Charbonneau et al. (2009), we present both the conversion of values cited by them and the transit times derived from our light curve fit to their data in Table 4 (see columns “Charbonneau et al. 2009,” and “chain003a”). We chose to use the times which resulted from our analysis (chain003a) since we fit for many transits simultaneously. These BJD<sub>TDB</sub> times are not far off from the converted transit times. The largest discrepancy we found was  $\sim 15$  s for the transit  $T_1$ . This difference is not surprising since it is the very first transit observed by Charbonneau et al. (2009) with a single MEarth telescope and hence has the least precise measurement ( $\sigma \sim 40$  s). Using all available transit times, we refit the ephemeris for GJ 1214b, with the first APOSTLE transit ( $T_7$ ) as the zeroth transit

$$TT(N_{Ti}) = T_{ZP} + P \times N_{Ti}, \quad (7)$$

where TT is the expected transit time,  $T_{ZP}$  is the zero-point of the transit times,  $P$  is the orbital period, and  $N_{Ti}$  is the transit number. Given all the times and transit numbers, we fit for  $T_{ZP}$  and  $P$ , and found them to be  $2455307.892474 \pm 0.000082$  BJD<sub>TDB</sub>, and  $1.58040487 \pm 0.00000067$  days, respectively. In Figure 5, we show the observed minus calculated ( $O - C$ ) transit times; there are no significant variations from the expected times of transit. The ephemeris fit produced a  $\chi^2 = 6.36$  given 12 dof.

If this system does have additional planets they may induce variations in transit times (Agol et al. 2005; Holman & Murray 2005). For the special case where these additional planets are in mean motion resonance (MMR) with GJ 1214b, the resulting TTVs could be on the order of minutes and well above the precision limits of transit follow-up surveys (see also Carter et al. 2011). A timing variation signal on the order of  $\sim 1$  minute could reveal approximately moon-mass perturbers in a 2:1 MMR (Agol et al. 2005, from Equation (33)). However, such a signal does not seem to exist (Figure 5). A null result however can be used to place interesting limits on the mass and orbital configurations of a possible undetected companion (Steffen

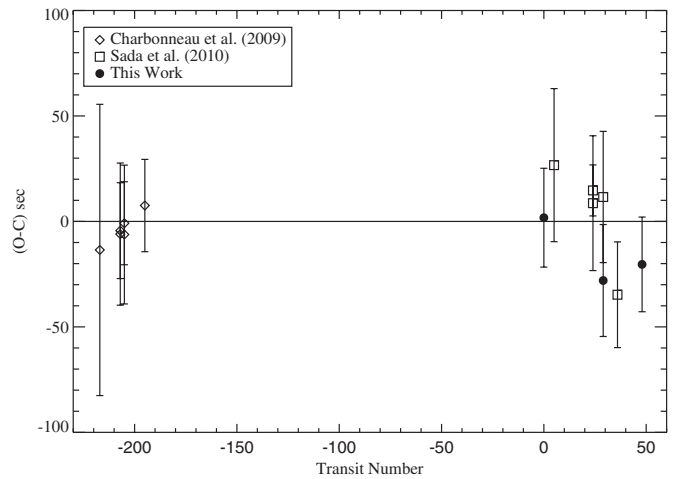


**Figure 5.** Observed minus calculated ( $O - C$ ) transit times vs. transit number for GJ 1214b. All transit times were converted to TDB. The Charbonneau et al. (2009) times are from our analysis of the joint APOSTLE and MEarth data set. The Sada et al. (2010) data were converted to BJD<sub>TDB</sub>.

& Agol 2005; Agol & Steffen 2007). We will defer such an analysis until more data are available, as GJ 1214 remains part of APOSTLE’s observing program.

#### 5. ABSOLUTE STELLAR AND PLANETARY PROPERTIES

Transit and RV data when taken together allow us to constrain various planetary parameters. However, many of these directly depend on the estimate of absolute stellar parameters, the most important being absolute stellar mass and radius. Transit light curves allow us to constrain the average stellar density ( $\rho_\star$ ). We can rewrite Kepler’s third law to get an expression of stellar density  $\rho_\star = 3\pi(a/R_\star)^3/(GP^2)$ , where  $G$  is the universal gravitational constant (Seager & Mallén-Ornelas 2003). The parameters,  $a/R_\star$  (the semimajor axis of the planet in stellar radius units) and  $P$  (the orbital period), can be deduced from transit data (see Section 3.3, Carter et al. 2008). To translate this measurement into an estimate of absolute mass and radius an additional constraint is required.

Stellar mass can be obtained using empirical or theoretical mass–luminosity relations of stars. However, given the stellar density measurement, one may also constrain mass and radius from the locus of points where the measured density (from transits) intersects with well-known stellar mass–radius relations. Mass–radius relations provide an understanding of the internal structures of stars. For stars in the mass range of GJ 1214, empirical mass–radius relations are difficult to interpret due to biases in the survey sample and large uncertainties in the measurement of stellar parameters. Theoretical considerations of internal structure show that the overall size of a star might be strongly affected by convection and magnetic activity (Chabrier et al. 2007). Mass–luminosity relations on the other hand stem from our understanding of the energy production in stars. Energy production rates from nuclear fusion in the core are better understood and hence the luminosity of low-mass stars relate better with mass (Chabrier & Baraffe 1997; Hillenbrand & White 2004). In light of this, we describe the derivation of absolute stellar properties of GJ 1214 using mass–luminosity relations. Once the stellar mass is obtained, getting the stellar radius is trivial, since  $\rho_\star = 3M_\star/(4\pi R_\star^3)$ . This method of estimating stellar density is applicable only under the assumption that the planetary

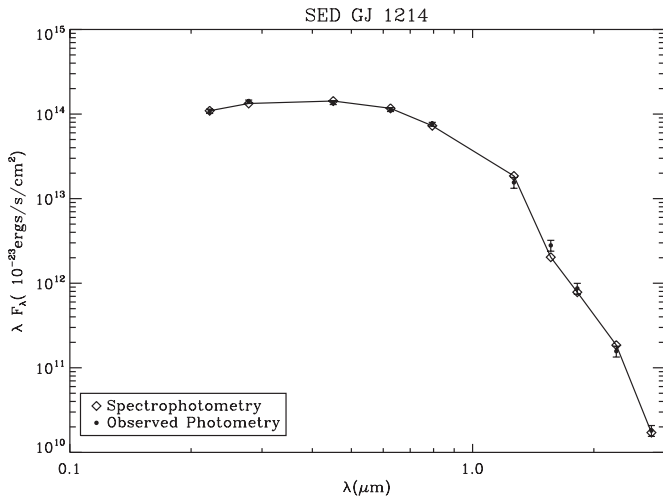


**Figure 6.** SED of GJ 1214 and the resulting best-fit spectrophotometry as described in Section 5. The photometric errors on the optical (UBVRI) data were adjusted to 15%, while those for the infrared data (Two Micron All Sky Survey and Warm *Spitzer*) were adjusted to 5%.

orbit is circular (Seager & Mallén-Ornelas 2003). We also discuss how the derived radius of GJ 1214 compares to well-known mass–radius relations of low-mass stars. Once the absolute stellar parameters are obtained, various measurements from RV and transit observations can be used to derive absolute parameters of GJ 1214b.

### 5.1. Stellar Mass and Radius

Photometry is available in eight wavebands (UBVRIJK) for GJ 1214 (Dawson & Forbes 1992; Skrutskie et al. 2006). We also obtained unpublished IRAC1 and IRAC2 flux estimates from J.-M. Désert (2010, private communication). Together these data cover the peak of GJ 1214’s spectral energy distribution (SED). This allowed us to fit the observed SED with spectrophotometry (derived using the technique described in Ivezić et al. 2007; Maíz Apellániz 2006) of model spectra (Hauschildt et al. 1999). The errors on the optical photometry were increased to 15% and the infrared data to 5% to compensate for inaccuracies in spectrophotometry. We fit for the effective temperatures ( $T_{\text{eff}}$ ) and  $\log g$  over the model grid. In addition, we fit for a constant,  $R_*/d$ , the ratio of the stellar radius to the distance of the star from Earth. This factor is related to the solid angle of the star and scales the synthetic spectra to the observed fluxes. Our best fit produced a  $\chi^2$  of 10.5 given 7 dof (see Figure 6). The uncertainties on the fit parameters were computed using the MCMC technique described in Section 3.2. Results from the MCMC run are shown in Figure 7. We integrated the resulting best-fit spectra (extracted at the best-fit  $T_{\text{eff}}$  and  $\log g$  on the grid) over all wavelengths and scaled it with the solid angle to derive the observed flux ( $F_{\text{obs}}$ ). We then used the parallax of  $77.2 \pm 5.4$  mas (van Altena et al. 1995) and estimated GJ 1214’s bolometric luminosity to be  $L_* = 0.0028 \pm 0.0004 L_\odot$ . Parameter values and uncertainties for all fit and derived parameters are quoted in Table 5. The MCMC points from the fit parameters were used to compute an ensemble of points for various derived parameters and these distributions were used to compute the errors on all derived parameters (see also Section 3.2). Working backwards from stellar properties, we recomputed fit parameters  $T_{\text{eff}} = 2913 \pm 72$  K,  $\log g = 4.981 \pm 0.009$ , and  $R_*/d = 0.0163 \pm 0.0008 R_\odot \text{pc}^{-1}$ , all of which are consistent with values from our fit.

**Table 5**  
Properties of GJ 1214 and GJ 1214b

Parameter	Value	Units
Fit SED Parameters		
$T_{\text{eff}}$	$2949^{+27}_{-32}$	K
$\log g$	$4.94^{+0.22}_{-0.26}$	$\log \text{cm s}^{-2}$
$R_*/d$	$0.0155 \pm 0.0003$	$R_\odot \text{pc}^{-1}$
Derived Stellar Parameters		
$F_{\text{obs}}$	$5.23 \pm 0.13$	$10^{-10} \text{erg s}^{-1} \text{cm}^{-2}$
$L_*$	$0.0028 \pm 0.0004$	$L_\odot$
$M_*$	$0.153^{+0.010}_{-0.009}$	$M_\odot$
$R_*$	$0.210^{+0.005}_{-0.004}$	$R_\odot$
Derived Planetary Parameters		
$M_p$	$6.37 \pm 0.87$	$M_\oplus$
$R_p$	$2.74^{+0.06}_{-0.05}$	$R_\oplus$
$\rho_p$	$1.68 \pm 0.23$	$\text{g cm}^{-3}$
$g_p$	$8.24 \pm 1.09$	$\text{m s}^{-2}$
$V_{\text{esc,p}}$	$12.03 \pm 0.80$	$\text{km s}^{-1}$
$T_{\text{eq}}$ (Bond albedo = 0)	$547^{+7}_{-8}$	K
$T_{\text{eq}}$ (Bond albedo = 0.75)	$387^{+5}_{-6}$	K

With an estimate of  $L_*$ , theoretical or empirical mass–luminosity relations can be used to estimate the stellar mass. We used data presented by Baraffe et al. (1998) for solar metallicity stars at an age of 5 Gyr and found GJ 1214 to have a mass  $M_* = 0.153 \pm 0.010 M_\odot$ . GJ 1214’s age is assumed to lie somewhere between 3 and 10 Gyr since its measured kinematics place it in the old disk population (Reid et al. 1995). The spread in mass–luminosity over this age range is insignificant ( $\ll 1\%$ ), so mass and luminosity data from the 5 Gyr isochrone served very well. GJ 1214’s metallicity has not been directly measured, but indirect means indicate that  $[\text{Fe}/\text{H}] > 0.0$ . For example, photometric proxies indicate that its  $[\text{Fe}/\text{H}] = +0.03$  or  $+0.28$  (Johnson & Apps 2009; Schlafman & Laughlin 2010, respectively). Rojas-Ayala et al. (2010) use near-IR equivalent widths of NAI, CaI, and the H<sub>2</sub>O index (Covey et al. 2010) for M dwarfs with and without planets to derive a spectroscopic metallicity indicator for M dwarfs. Using this method they report an  $[\text{Fe}/\text{H}] = +0.39$ . The Baraffe et al. (1998) models unfortunately do not cover this high-metallicity range, so as a check we also estimate the stellar mass using an empirical mass–luminosity function presented by Scalo et al. (2007). This fit is based on masses derived from observations of binary stars (Hillenbrand & White 2004), and the sample should represent a wide range of metallicities. Using this fit, we derived  $M_* = 0.148 M_\odot$ , which is  $0.005 M_\odot$  lower than the value derived from the theoretical relation, but well within the uncertainties. Charbonneau et al. (2009) adopt a similar technique, but use a mass–luminosity function calibrated for mid-infrared *K*-band luminosities to determine the mass (Delfosse et al. 2000). Their estimate of the mass was  $0.157 \pm 0.019 M_\odot$  and is consistent with our measurement. We estimated the stellar radius and its error using the stellar density from “chain003a” and the ensemble of derived stellar mass points. Figure 8 shows stellar mass versus radius. The two dash-dotted curves on the plot (shown in red and blue in the color version) are the  $1\sigma$  contours of constant stellar density obtained from transit observations in this work (“chain003a”) and Charbonneau et al. (2009), respectively. The uncertainty in stellar radius spans the region between these contours for a given stellar mass.

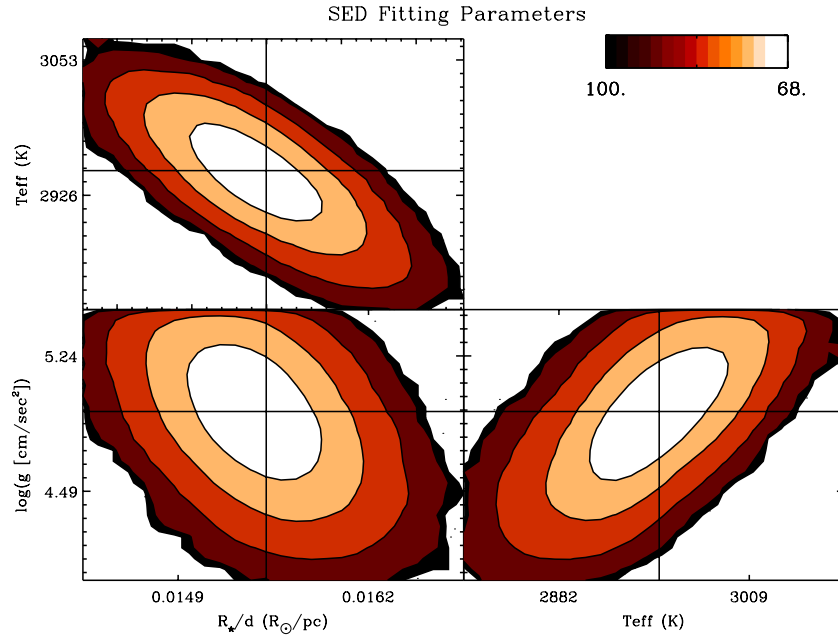


**Figure 7.** Joint probability distributions for the three parameters used for SED fitting. The numbers and units correspond to those listed in Table 5. The solid line crosshairs mark the location of the best-fit values (also from Table 5). The contours mark the  $1\sigma$ ,  $2\sigma$ ,  $3\sigma$ ,  $4\sigma$  and  $5\sigma$  regions, each enclosing 68.27%, 95.45%, 99.73%, 99.994%, and 99.99994% of the points in the distributions, respectively.

(A color version of this figure is available in the online journal.)

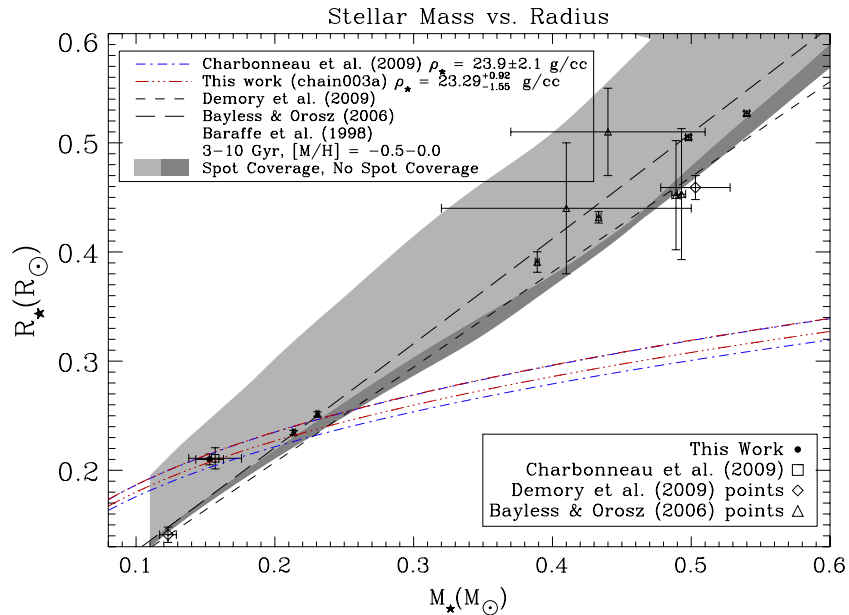


**Figure 8.** Stellar mass ( $M_*$ ) vs. stellar radius ( $R_*$ ), in solar units. The linestyles are matched to their corresponding references in the legend on the top left corner of the figure and the legend on the bottom right matches the data points on the plot. The two dashed lines in black are empirically derived mass–radius relations for low-mass main-sequence stars (Demory et al. 2009; Bayless & Orosz 2006). The data points are various estimates of mass and radius. The estimates of mass and radius presented in this work and Charbonneau et al. (2009) are also marked on the plot. The two dash-dotted curves, shown in red and blue in the color version, are the  $1\sigma$  contours of constant stellar density obtained from transit observations in this work and Charbonneau et al. (2009), respectively. The shaded regions represent the spread in stellar mass and radius taking into account various theoretical considerations. The darker region represents the spread over age (3–10 Gyr) and metallicity (–0.5–0.0) for stars without spots. The lighter region shows this spread when spot-coverage is introduced using the formalism of Chabrier et al. (2007). The outer limit (leftmost edge) of the light region represents the case of 65% area coverage of spots which are 1000 K cooler than the fiducial surface temperature of the star for a given mass (Morales et al. 2010).

(A color version of this figure is available in the online journal.)

Figure 8 shows that our estimates for the mass and radius of GJ 1214 do not lie close to the empirical mass–radius relations for low-mass stars (Demory et al. 2009; Bayless & Orosz 2006); the empirical relations are represented by the dashed lines in the figure. Our estimate is also far from the dark shaded region on the

figure, which shows the spread in mass and radius due to a range of metallicities and ages from theoretical models (Baraffe et al. 1998). Chabrier et al. (2007) discuss how the internal structure of low-mass stars is affected by magnetic activity and convection. For example, the overall sizes of stars might be affected by cool

**Table 6**  
APOSTLE Light Curve (UTD 2010 April 21)

BJD–Mid Transit Time (d)	Normalized Flux Ratio	Errors on Normalized Flux Ratio	Model Light Curve
–0.079827555797	1.001194412071	0.001156237274	1.000000000000
–0.079306689397	1.000339471196	0.001165426669	1.000000000000
–0.075799521393	1.001362190427	0.001159162883	1.000000000000
–0.075278654993	0.998706244091	0.001181295967	1.000000000000
–0.074757788199	0.999322538904	0.001171937351	1.000000000000
–0.074236921799	0.997417501319	0.001170175533	1.000000000000
–0.073716055398	0.999676247486	0.001164536618	1.000000000000
–0.073195188597	0.997863667333	0.001144023943	1.000000000000
–0.072674322299	0.996991199650	0.001189910735	1.000000000000
–0.072153455898	0.998682374021	0.001171293203	1.000000000000
–0.071632589497	1.001395055990	0.001137204356	1.000000000000
–0.071111722697	0.998433944852	0.001130410838	1.000000000000
–0.070590856296	1.000377434388	0.001131055589	1.000000000000

**Note.** Entire APOSTLE light curves are provided in the online version of the journal.

(This table is available in its entirety in a machine-readable form in the online journal. A portion is shown here for guidance regarding its form and content.)

spots on the surface where magnetic field lines penetrate deep into the convective layer. This situation can reduce the efficiency of convective energy transport, causing the star to settle to a larger radius for a given luminosity and fiducial temperature (Morales et al. 2010). Figure 8 shows the region bounded by extreme spot-coverage as the light shaded region. Note that this curve is purely hypothetical and introducing spot-coverage is equivalent to choosing a lower effective temperature for a given mass.<sup>2</sup> Our derived absolute parameters fall within the light shaded region, which suggests that GJ 1214 has cool regions on its surface. We discuss some evidence for spots and magnetic activity in a subsequent section (Section 6). Addressing spotting and convection in detail is beyond the scope of this paper.

An alternate explanation for the discrepancy could be the estimate of GJ 1214’s luminosity. If empirical mass–radius relations are to be believed, GJ 1214’s mass and radius would be closer to  $0.23 M_{\odot}$  and  $0.24 R_{\odot}$ , based on the intersection with the density contours. Working backwards, this translates to a bolometric luminosity of roughly  $0.0065 L_{\odot}$ . This is a very large difference in luminosity from the current estimate and can only be reconciled with the observed fluxes if the star was further away by 7 pc (i.e., a parallax that was smaller by  $0''.027$  than the current estimate). The discrepant measurement would have to be a  $5\sigma$  systematic error and hence highly unlikely.

### 5.2. Absolute Planetary Parameters

With the semi-amplitude from RV ( $K = 12.2 \pm 1.6 \text{ m s}^{-1}$ ; Charbonneau et al. 2009), and the period ( $P$ ) and inclination from transit observations, one can determine the planetary mass using:  $K \propto M_p \sin i / (M_{\star}^{2/3} P^{1/3})$ . The planetary radius can be determined from the planet-to-star radius ratio measured from the transit light curve. The density ( $\rho_p$ ), escape velocity ( $V_{\text{esc,p}}$ ), and surface gravity ( $g_p$ ) can then be derived from the planet’s mass and radius. Using the semimajor axis ( $a/R_{\star}$ ),  $R_{\star}$ , and stellar effective temperature ( $T_{\text{eff}}$ ), we estimated the equilibrium temperature of the planet to be  $547_{-8}^{+7}$  K and  $387_{-6}^{+5}$  K assuming Bond albedos of 0.0 and 0.75, respectively. All errors were propagated assuming Gaussian uncertainties. We list our

estimates in Table 5. The planetary mass, radius, and density, we derive are  $M_p = 6.37 \pm 0.87 M_{\oplus}$ ,  $R_p = 2.74_{-0.05}^{+0.06} R_{\oplus}$ , and  $\rho_p = 1.68 \pm 0.23 \text{ g cm}^{-3}$ , respectively. These data confirm GJ 1214b’s status as a super-Earth, and the density measurement attests the presence of a massive gas envelope. The inner edge of the habitable zone for GJ 1214 would lie roughly at 0.027 AU (based on Selsis et al. 2007, 100% cloud cover). GJ 1214b is not situated in the habitable zone as its semimajor axis ( $\sim 0.014$  AU) lies inside the inner edge. Lower cloud coverage fractions would only push the inner edge further out.

## 6. STELLAR ACTIVITY

Many main-sequence stars are believed to be magnetically active and the frequency of active stars is known to increase with decreasing mass. Most observed variability on such stars is likely due to star spots and stellar flares (Basri et al. 2010; Walkowicz et al. 2011). The evidence for spots on the stellar surface is inferred from rotationally modulated long-term periodic trends in stellar light curves. Flares on the other hand are short-term events which are believed to be caused by the sudden release of energy from the reconnection of magnetic field lines near an active surface region. Some of the most active M dwarfs are believed to lie at masses below the transition between partially and fully convective interiors ( $< 0.35 M_{\odot}$ ; Reiners & Basri 2009). The increased activity is often thought to be a result of asymmetric magnetic field topologies for fully convective low-mass stars. Although GJ 1214 ( $0.153 M_{\odot}$ ) lies well within this mass range, it has been classified as an inactive M dwarf by Hawley et al. (1996) based on an  $H\alpha$  activity index. Active stars are bound to have numerous cool or hot regions on their surface; the existence of such regions can be inferred from the detection of spot or flare features in light curves. We believe that our  $r$  band observations show evidence for a low-energy stellar flare on GJ 1214 and the possible eclipse of a cool spot on the stellar surface by the planet.

The sharp rising and falling trend seen in the out-of-eclipse light curve on UTD 2010 April 21 (Figure 1) is similar to the fast-rise exponential decay (FRED) shape commonly associated with stellar flares (Hawley & Pettersen 1991). Panel (a) in Figure 9 shows this event in greater detail. We built a light curve model with two components: (1) a linear rise phase and (2) an exponential decay phase. We fit for the start time, peak time,

<sup>2</sup> The Chabrier et al. (2007) formalism only attempts to analytically convey the effects that spot-coverage and convective efficiency have on the structure of low-mass stars.

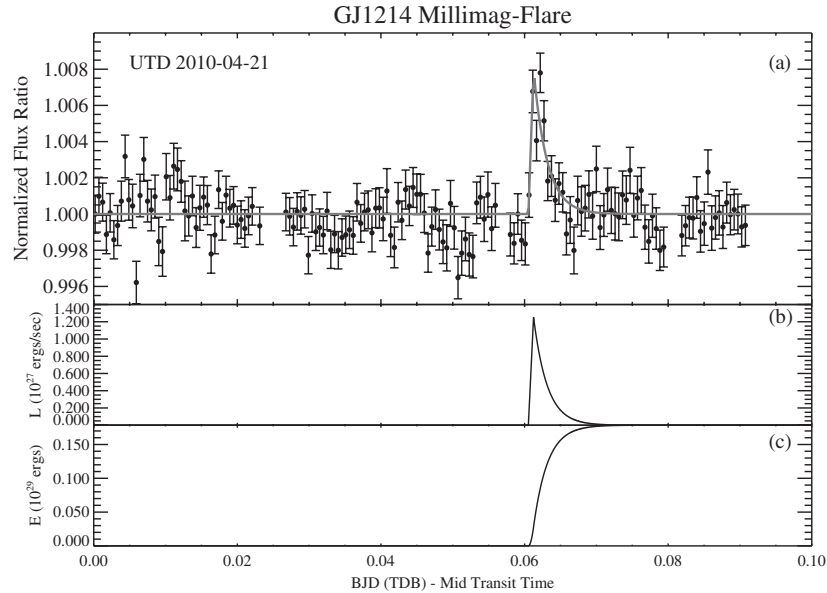


**Figure 9.** (a) Shows the flare event observed on UTD 2010 April 21. The data are the same as those shown in Figure 1(b), only magnified. The gray line is the best-fit FRED model. Even though only the points after mid-transit are shown, the fit was made using all light curve points (in Figure 1(b)). Panel (b) in the above figure shows the  $r$ -band luminosity as a function of time and panel (c) shows the total energy output by the flare above the quiescent  $r$ -band level as a function of time.

peak flux, and the  $e$ -folding time of the exponential phase. The best-fit light curve is shown as the solid gray line in Figure 9(a). The  $\Delta\chi^2$  for this flare model compared to a straight line fit to the data is 112.6. The  $r$  band flux of the star rose to a peak 0.8% above the quiescent level and decayed over  $\sim 3$  minutes ( $e$ -folding time). Since we lacked flux-calibrated photometry, we used synthetic stellar spectra (Hauschildt et al. 1999) to estimate the energy output by this event. We determined the  $r$ -band flux by integrating the synthetic spectra of a star with  $T_{\text{eff}} = 2949$  K and  $\log g = 4.94$  over the spectral response of the  $r$  band (Ivezić et al. 2007; Maíz Apellániz 2006). Using a stellar radius of  $0.21 R_{\odot}$ , we computed the quiescent luminosity in the  $r$  band to be  $\sim 1.6 \times 10^{29} \text{ erg s}^{-1}$ . Panel (b) shows our flare model in luminosity units above the quiescent level for GJ 1214. Following the method described in Hawley et al. (2003) and Kowalski et al. (2010), we integrated under the flare light curve and estimated the total energy output by the flare in the  $r$  band to be  $\sim 1.8 \times 10^{28} \text{ erg}$ ; see Figure 9(c). The time it would take for the non-flaring star to emit this amount of energy (referred to as the equivalent time in the M dwarf flare community) is 0.113 s. Compared to typical M dwarf flares, this event is short-lived and of much lower energy. In fact such events are likely to be drowned out by noise for most flare monitoring campaigns as millimagitude precision is not commonly desired when looking at the most active stars. Hawley et al. (2003) reported flare energies between  $8 \times 10^{30}$  and  $58 \times 10^{30} \text{ erg}$  from Johnson  $R$  filter observations of the active star AD Leonis. The activity observed on GJ 1214 is four orders of magnitude lower in energy than some of the energetic flares observed on AD Leo (also an M4.5V star). AD Leo has been identified as a member of the young galactic disk population (Montes et al. 2001). West et al. (2008) have established that stellar activity decreases with age, and hence the differences in the activity levels of GJ 1214 and AD Leo might be purely due to the differences in their ages.

During the transit on UTD 2010 June 6, we observed a slight brightening in the light curve at the onset of egress (see Figure 1). Figure 10 shows this event in greater detail. The flare model described above provided poor fits to this signal; the shape seen is far more symmetric than the FRED shape of a

flare. The symmetry and the fact that it occurred during transit makes it very likely that we observed a spot-crossing event. We modeled the spot-crossing signal based on the analytic expressions in Mandel & Agol (2002) for the area of intersection between two circles, assuming that the spot was of roughly circular shape. We did not account for the deformation of the spot due to the curvature of the star, and we assumed a zero spot-planet impact parameter. We fit for the spot-crossing duration, signal height, and central crossing time. The best-fit model is shown in Figure 10. The signal height is proportional to the square of the radius ratio of the spot to the planet ( $R_{sp}^2/R_p^2$ ) and also depends on the brightness contrast between the spot and the star (Silva 2003). For the limiting case of maximum spot-to-star contrast (a 0 K spot) we get a minimum spot radius of roughly  $0.17 R_{\oplus}$ . A more realistic spot-to-star temperature differential, such as 1000 K, can also produce contrast ratios high enough to reproduce the size estimate (see Silva 2003). Spots on the Sun are cooler than the surface by roughly 1000 K, but they can be of several Earth radii in size. The model shown in Figure 10 fits the feature better than a flat line, with a relative goodness of fit,  $\Delta\chi^2 = 32.6$ . The duration of spot crossing ( $t_{T,sp}$ ) can also be used to estimate the longitudinal extent of the cool region as,  $l_{sp} \propto 2R_{sp} \propto t_{T,sp}a/\text{period}$ . For a duration  $t_{T,sp} \approx 180$  s, we get a spot radius of  $\sim 0.23 R_{\oplus}$  in the longitudinal direction (Rabus et al. 2009). The two spot size estimates are somewhat consistent, yet one must note that our calculations do not account for (1) the deformation of the spot and its latitudinal extent on the surface of the star, (2) we also do not account for non-zero impact parameters on spot crossing, and (3) due to a strong degeneracy with spot size we do not fit the spot temperature (contrast) as a free parameter. Recently, Carter et al. (2011) reported similar anomalies in their light curves of GJ 1214b, which they attributed to spots. Their analysis extended to quantifying the variations in transit depth over many epochs caused by spots. We refrain from such an analysis due to our limited data set. Detailed calculations of spot crossing have been made by long-term monitoring of active stars with planets, such as CoRoT-2, CoRoT-6, and CoRoT-7 (Lanza et al. 2009, 2010, 2011).

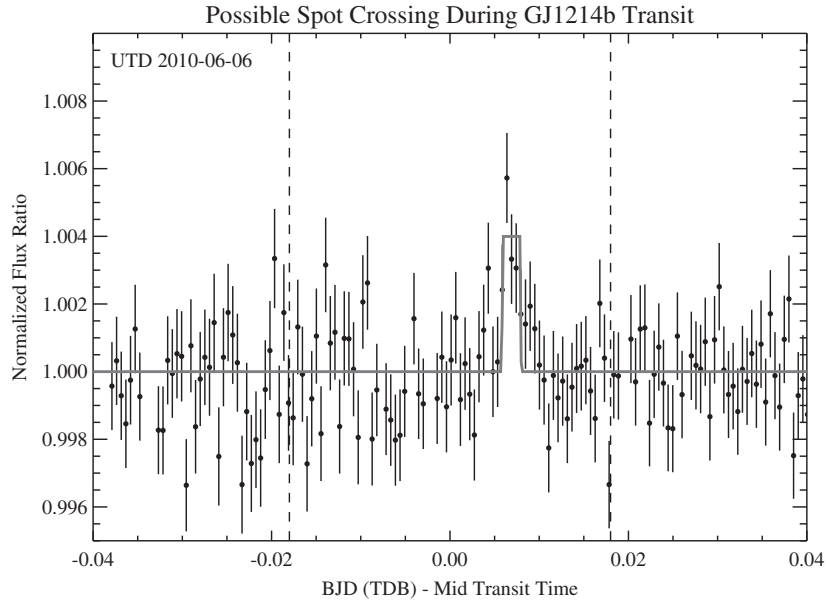


**Figure 10.** Possible spot-crossing event from the UTD 2010 June 6 transit of GJ 1214b. The transit signal was removed by normalizing the light curve with the best-fit transit model. The vertical dashed lines approximately mark the start and end of the transit. The gray line shows a fit using a simplified spot model.

## 7. CONCLUSIONS

**I. A Transit Model Suited for Bayesian Analysis.** A set of multi-wavelength lightcurves, which included three new lightcurves gathered by APOSTLE (presented in Figure 1 and Table 6) and other observations, were used in our Bayesian analysis. We show that fitting for the transit duration ( $t_T$ ) and the ingress/egress duration ( $t_G$ ) results in a parameter set with few mutual degeneracies (see Figure 2). This condition is suited very well for MCMC methods, which are regularly used to determine uncertainties on parameters derived from transit light curves. Our joint analysis of multi-wavelength data using this parameter set was able to reproduce previous estimates of system parameters for GJ 1214b (see Table 4, chain003a). We find that millimagnitude photometry may not be sufficient to constrain limb-darkening parameters using transit light curves (see also Southworth 2008). We show that MCMC runs where we fit for these parameters were slow to converge (see Table 2), and posterior probability distributions for various parameters were plagued with degeneracies (see Figure 3). Estimates of system parameters from these runs were generally unreliable when compared to runs where the limb-darkening parameters were kept fixed (see chains “b” versus “a” in Tables 3 and 4).

**II. Transit Timing Variations.** Data gathered so far do not indicate significant variations in the times of transit for GJ 1214b (see Figure 5). APOSTLE will continue making observations of GJ 1214b and a more detailed analysis of timing data will follow in a future paper.

**III. System Parameters for GJ 1214.** From fitting SEDs to photometry, we constrained GJ 1214’s observed flux and luminosity (Section 5). The luminosity allowed us to constrain GJ 1214’s mass and since we obtained stellar density from transit light curves it allowed us to estimate GJ 1214’s radius. We did not account for eccentric orbits, which may affect our density measurement and hence mass–radius estimate. We find the derived values of mass and radius to be in agreement with previous estimates; however, we find GJ 1214 deviates from well-known mass–radius relations for low-mass stars (see Figure 8). Simple calculations using the formalism presented in Chabrier et al. (2007) show that GJ 1214’s position on the

mass–radius plot can be explained by the presence of cool regions on its surface.

From RV, transit data (Charbonneau et al. 2009), and absolute stellar properties, we determined various properties of GJ 1214b (see Table 5). The planetary mass and radius ( $6.37 \pm 0.87 M_{\oplus}$ ,  $2.74^{+0.06}_{-0.05} R_{\oplus}$ ) place GJ 1214b between the terrestrial and ice-giant regime of planets ( $2 M_{\oplus} < M_p < 10 M_{\oplus}$ ). Our estimates are consistent with other recent reports (Sada et al. 2010; Carter et al. 2011; Berta et al. 2011). GJ 1214b’s classification as a ‘super-Earth’ remains and its density confirms that it is unlike the rocky bodies of our solar system (see Table 5). Rogers & Seager (2010) propose three scenarios for the origin of its gaseous envelope: (1) primordial H/He, (2) sublimated ices ( $H_2O$ ,  $CO_2$ ), or (3) volcanic outgassing. Miller-Ricci & Fortney (2010) propose that space-based observations of the transmission spectra of GJ 1214b’s atmosphere should be able to tell us how Hydrogen-rich its atmosphere is. The largest source of uncertainty in our estimate of planetary mass was the velocity semi-amplitude ( $K$ ). Errors in the planetary radius follow from our uncertainty in measuring the absolute size of the star, which ultimately hinges on our luminosity estimate (see Section 5). Improved precision on RV, flux, and distance would tighten our constraints on the absolute mass and radius of GJ 1214b.

**IV. Evidence for Stellar Activity.** The detection of a low-energy stellar flare and the possible transit of the planet over a star spot (see Figures 9 and 10) indicate that GJ 1214 is active. However, considering its age and comparing the flare energy to flares on the younger AD Leo confirms that GJ 1214 is a quiet star for its spectral type (Hawley et al. 1996, 2003). We find that a FRED profile fits the flare signal (UTD 2010 April 21) quite well.

A symmetric rise in the normalized flux ratio during the transit on UTD 2010 June 6 could indicate the planet occulted a star spot on the surface of GJ 1214. A simple model fit to this signal provided an estimate of minimum spot size  $R_{sp} \geq 0.17 R_{\oplus}$ . Detections of this signal from successive transits would have confirmed it as a star spot and provided interesting constraints on the properties of an active stellar surface region (Dittmann et al. 2009). The stellar rotation rate might have also been

estimated with such data. Spot-modulated light curves have been presented recently by Berta et al. (2011) as strong evidence for rotation. The agreement in temperature derived from SED fitting and the temperature estimated from our luminosity and radius measurements (Section 5.1) seems to indicate that the star is overall cooler than predicted by  $M-R$  relations, but probably does not have large areas with significant temperature contrasts. The spot-crossing event suggests that active regions are likely to be localized on the surface of the star.

Funding for this work came from NASA Origins grant NNX09AB32G and NSF Career grant 0645416. We thank an anonymous referee for reviewing our paper. We thank the APO Staff and Engineers for helping the APOSTLE program with its observations and instrument characterization. We thank S. L. Hawley and A. Kowalski for very helpful discussions on M dwarfs and stellar flares and J. Davenport for providing useful tips on contour plotting in IDL. A large part of our analysis depended on data from Charbonneau et al. (2009). We are indebted to the MEarth team (especially D. Charbonneau, Z. Berta, and P. Nutzman) for providing us their light curves. We are thankful to J. Eastman for a useful discussion on time coordinates and for parts of his transit model code written in PYTHON which were implemented in our analysis. We are also grateful to J.-M. Désert for providing us with tentative Warm *Spitzer* measurements of GJ 1214's flux.

## REFERENCES

- Agol, E., & Steffen, J. H. 2007, *MNRAS*, **374**, 941
- Agol, E., Steffen, J., Sari, R., & Clarkson, W. 2005, *MNRAS*, **359**, 567
- Baraffe, I., Chabrier, G., Allard, F., & Hauschildt, P. H. 1998, *A&A*, **337**, 403
- Baraffe, I., Chabrier, G., & Barman, T. 2008, *A&A*, **482**, 315
- Basri, G., et al. 2010, *ApJ*, **713**, 155
- Bayless, A. J., & Orosz, J. A. 2006, *ApJ*, **651**, 1155
- Berta, Z. K., Charbonneau, D., Bean, J., Irwin, J., Burke, C. J., Nutzman, P., Désert, J.-M., & Falco, E. E. 2011, *ApJ*, in press (arXiv:1012.0518)
- Bertin, E., & Arnouts, S. 1996, *A&AS*, **117**, 393
- Borucki, W. J., & Summers, A. L. 1984, *Icarus*, **58**, 121
- Brown, T. M., Charbonneau, D., Gilliland, R. L., Noyes, R. W., & Burrows, A. 2001, *ApJ*, **552**, 699
- Carter, J. A., Winn, J. H., Fabrycky, D., Berta, Z. K., Burke, C. J., & Nutzman, P. 2011, *ApJ*, **730**, 82
- Carter, J. A., Yee, J. C., Eastman, J., Gaudi, B. S., & Winn, J. N. 2008, *ApJ*, **689**, 499
- Chabrier, G., & Baraffe, I. 1997, *A&A*, **327**, 1039
- Chabrier, G., Gallardo, J., & Baraffe, I. 2007, *A&A*, **472**, L17
- Charbonneau, D., et al. 2009, *Nature*, **462**, 891
- Claret, A. 2004, *A&A*, **428**, 1001
- Collier Cameron, A., et al. 2007, *MNRAS*, **380**, 1230
- Covey, K. R., Lada, C. J., Román-Zúñiga, C., Muench, A. A., Forbrich, J., & Ascenso, J. 2010, *ApJ*, **722**, 971
- Dawson, P. C., & Forbes, D. 1992, *AJ*, **103**, 2063
- Delfosse, X., Forveille, T., Ségransan, D., Beuzit, J.-L., Udry, S., Perrier, C., & Mayor, M. 2000, *A&A*, **364**, 217
- Demory, B.-O., et al. 2009, *A&A*, **505**, 205
- Dittmann, J. A., Close, L. M., Green, E. M., & Fenwick, M. 2009, *ApJ*, **701**, 756
- Eastman, J., Siverd, R., & Gaudi, B. S. 2010, *PASP*, **122**, 935
- Edwards, R. T., Hobbs, G. B., & Manchester, R. N. 2006, *MNRAS*, **372**, 1549
- Ford, E. B. 2005, *AJ*, **129**, 1706
- Fortney, J. J., Lodders, K., Marley, M. S., & Freedman, R. S. 2008, *ApJ*, **678**, 1419
- Fukugita, M., Ichikawa, T., Gunn, J. E., Doi, M., Shimasaku, K., & Scheider, D. p. 1996, *AJ*, **111**, 1748
- Gelman, A., et al. 2003, *Bayesian Data Analysis* (2nd ed.; Boca Raton, FL: Chapman & Hall/CRC)
- Gillon, M., Bonfils, X., Demory, B.-O., Seager, S., Deming, D., & Triaud, A. H. M. J. 2011, *A&A*, **525**, A32
- Guillot, T. 2005, *Annu. Rev. Earth Planet. Sci.*, **33**, 493
- Hauschildt, P. H., Allard, F., & Baron, E. 1999, *ApJ*, **512**, 377
- Hawley, S. L., Gizis, J. E., & Reid, I. N. 1996, *AJ*, **112**, 2799
- Hawley, S. L., & Pettersen, B. R. 1991, *ApJ*, **378**, 725
- Hawley, S. L., et al. 2003, *ApJ*, **597**, 535
- Hillenbrand, L. A., & White, R. J. 2004, *ApJ*, **604**, 741
- Hobbs, G. B., Edwards, R. T., & Manchester, R. N. 2006, *MNRAS*, **369**, 655
- Holman, M. J., & Murray, N. W. 2005, *Science*, **307**, 1288
- Holman, M. J., et al. 2006, *ApJ*, **652**, 1715
- Ikoma, M., Emori, H., & Nakazawa, K. 2001, *ApJ*, **553**, 999
- Ivezić, Ž., et al. 2007, *AJ*, **134**, 973
- James, F. 1994, CERN Program Library Long Writeup D506
- Johnson, J. A., & Apps, K. 2009, *ApJ*, **699**, 933
- Joshi, M. M., Haberle, R. M., & Reynolds, R. T. 1997, *Icarus*, **129**, 450
- Kasting, J. F., Whitmire, D. P., & Reynolds, R. T. 1993, *Icarus*, **101**, 108
- Kowalski, A. F., Hawley, S. L., Holtzman, J. A., Wisniewski, J. P., & Hilton, E. J. 2010, *ApJ*, **714**, L98
- Lanza, A. F., et al. 2009, *A&A*, **493**, 193
- Lanza, A. F., et al. 2010, *A&A*, **520**, A53
- Lanza, A. F., et al. 2011, *A&A*, **525**, A14
- Léger, A., et al. 2009, *A&A*, **506**, 287
- Lissauer, J. J., Hubickyj, O., D'Angelo, G., & Bodenheimer, P. 2009, *Icarus*, **199**, 338
- Maíz Apellániz, J. 2006, *AJ*, **131**, 1184
- Mandel, K., & Agol, E. 2002, *ApJ*, **580**, L171
- Miller, G. E., & Scalo, J. M. 1979, *ApJS*, **41**, 513
- Miller-Ricci, E., & Fortney, J. J. 2010, *ApJ*, **716**, L74
- Monet, D. G., et al. 2003, *AJ*, **125**, 984
- Montes, D., López-Santiago, J., Gálvez, M. C., Fernández-Figueroa, M. J., De Castro, E., & Cornide, M. 2001, *MNRAS*, **328**, 45
- Morales, J. C., Gallardo, J., Ribas, I., Jordi, C., Baraffe, I., & Chabrier, G. 2010, *ApJ*, **718**, 502
- Nather, R. E., & Mukadam, A. S. 2004, *ApJ*, **605**, 846
- Pollack, J. B., Hubickyj, O., Bodenheimer, P., Lissauer, J. J., Podolak, M., & Greenzweig, Y. 1996, *Icarus*, **124**, 62
- Pont, F., et al. 2007, *A&A*, **476**, 1347
- Queloz, D., et al. 2009, *A&A*, **506**, 303
- Rabus, M., et al. 2009, *A&A*, **494**, 391
- Reid, I. N., Gizis, J. E., & Hawley, S. L. 2002, *AJ*, **124**, 2721
- Reid, I. N., Hawley, S. L., & Gizis, J. E. 1995, *AJ*, **110**, 1838
- Reiners, A., & Basri, G. 2009, *A&A*, **496**, 787
- Rogers, L. A., & Seager, S. 2010, *ApJ*, **716**, 1208
- Rojas-Ayala, B., Covey, K. R., Muirhead, P. S., & Lloyd, J. P. 2010, *ApJ*, **720**, L113
- Sada, P. V., et al. 2010, *ApJ*, **720**, L215
- Scalo, J., et al. 2007, *Astrobiology*, **7**, 85
- Schlaufman, K. C., & Laughlin, G. 2010, *A&A*, **519**, A105
- Seager, S., & Mallén-Ornelas, G. 2003, *ApJ*, **585**, 1038
- Seidelmann, P. K., & Fukushima, T. 1992, *A&A*, **265**, 833
- Selsis, F., Kasting, J. F., Levrard, B., Paillet, J., Ribas, I., & Delfosse, X. 2007, *A&A*, **476**, 1373
- Silva, A. V. R. 2003, *ApJ*, **585**, L147
- Skrutskie, M. F., et al. 2006, *AJ*, **131**, 1163
- Southworth, J. 2008, *MNRAS*, **386**, 1644
- Standish, E. M. 1998, *A&A*, **336**, 381
- Steffen, J. H., & Agol, E. 2005, *MNRAS*, **364**, L96
- Tegmark, M., et al. 2004, *Phys. Rev. D*, **69**, 103501
- Torres, G., Winn, J. N., & Holman, M. J. 2008, *ApJ*, **677**, 1324
- van Altena, W. F., Lee, J. T., & Hoffleit, E. D. 1995, *The General Catalogue of Trigonometric (Stellar) Parallaxes* (4th ed.; New Haven, CT: Yale Univ. Observatory)
- Walkowicz, L. M., et al. 2011, *AJ*, **141**, 50
- West, A. A., Hawley, S. L., Bochanski, J. J., Covey, K. R., Reid, I. N., Dhital, S., Hilton, E. J., & Masuda, M. 2008, *AJ*, **135**, 785
- Winn, J. N., Holman, M. J., & Roussanova, A. 2007, *ApJ*, **657**, 1098